Scientific Reports

https://doi.org/10.1038/s41598-026-44959-7

Article in Press

Macroscopic polarimetric discrimination and quantification of antiangiogenic effect of AGRO aptamer and GK1 peptide in a preclinical melanoma model

Received: 13 November 2025

Accepted: 16 March 2026

Published online: 20 March 2026

Cite this article as: Montes-Gonzalez I., Bisbal-Amat J., Perez-Torres A. *et al.* Macroscopic polarimetric discrimination and quantification of antiangiogenic effect of AGRO aptamer and GK1 peptide in a preclinical melanoma model. *Sci Rep* (2026). https://doi.org/10.1038/s41598-026-44959-7

Ivan Montes-Gonzalez, Judit Bisbal-Amat, Armando Perez-Torres, Evelyn Pulido-Camarillo, Monica Canabal-Carbia, juan Campos, Irene Estevez & Angel Lizana

Macroscopic polarimetric discrimination and quantification of antiangiogenic effect of AGRO aptamer and GK1 peptide in a preclinical melanoma model

IVAN MONTES-GONZALEZ,[1*,] JUDIT BISBAL-AMAT,[1,] ARMANDO PEREZ-TORRES,[2*,] EVELYN PULIDO-CAMARILLO,[2,] MONICA CANABAL-CARBIA,[1,] JUAN CAMPOS,[1,] IRENE ESTEVEZ,[1,] AND ANGEL LIZANA[1*,]

[1]*Optics Group, Physics Department, Universitat Autonoma de Barcelona, Bellaterra 08193, Spain*
[2] *Cellular and Tissue Biology Department, Faculty of Medicine, Universidad Nacional Autonoma de México, Ciudad de México 04510, México.*
**montes_ivan@yahoo.com / armandop@unam.mx/ angel.lizana@uab.cat*

Abstract: Histological analysis remains the gold standard for tissue diagnosis and evaluation, but it often relies on subjective visual interpretation and limited field of view areas. In this study, we present a macroscopic, wide-field Mueller polarimetric imaging approach for the quantitative analysis of histological sections of melanoma induced with the B16F10 cell line in mice. By using the depolarization index, our method enables objective tissue discrimination based on intrinsic tissue properties. A color-coded segmentation mask derived from the depolarization index values was implemented to classify tissue into strongly depolarizing regions, associated with blood vessels, and weakly depolarizing regions, which predominantly correspond to tumor cell–dominated tissue. This pixel-wise classification allowed for quantitative mapping and statistical analysis of spatial heterogeneity across several mm^2 of entire histological sections, significantly extending the field of view compared to conventional microscopy.

As a potential application, the technique was applied to evaluate histological sections from a preclinical murine melanoma model subjected to a treatment regimen including antiangiogenic agents. The results demonstrated measurable differences in the amount of strongly depolarizing tissue, associated with blood vessels, in the treatment group, supporting the method's sensitivity to antiangiogenic effects in the tumor microenvironment. These findings highlight the potential of Mueller polarimetry as a complementary tool for histological assessment, enabling reproducible, large-area tissue characterization beyond visual inspection.

Introduction

Cancer comprises a group of over 100 distinct diseases characterized by dysregulated cell growth and control of the cell cycle. This disruption is often driven by genetic mutations that activate oncogenes or inactivate tumor suppressor genes, leading to impaired differentiation, uncontrolled proliferation, and resistance to apoptosis [1]. Tumor cells also acquire invasive capabilities and disseminate to surrounding tissues and distant organs, resulting in metastasis. A hallmark of all tumors is the development of a heterogeneous and dynamic microenvironment that supports tumor survival, immune evasion, and angiogenesis. Newly formed blood vessels not only nourish the cancer but also facilitate metastatic spread [2-4].

Among skin cancers, melanoma is the most aggressive and deadly skin cancer type. According to an epidemiological assessment of global cancer data, 325,000 new melanoma cases (174,000 males, 151,000 females) and 57,000 deaths (32,000 males, 25,000 females) occurred due to melanoma in 2020, with large geographic variations in incidence across countries and world regions. Incidence increment is observed in fair-skinned populations of European descent, but continued to be rare in most African and Asian countries, with incidence rates commonly less than 1 per

100,000 person-years. If 2020 melanoma rates remain stable, the global burden from melanoma is estimated to increase to 510,000 new cases and 96,000 deaths by 2040 [5].

Melanoma angiogenesis is a central indicator of metastasis and poor patient survival, remaining a major clinical challenge despite significant advances in cancer diagnosis and treatment [6]. Tumor progression, angiogenesis, and metastasis are not solely driven by tumor cells but also result from complex interactions within the tumor microenvironment (TME), involving immune and non-immune cells, as well as fibrous and non-fibrous components of the extracellular matrix [7]. In the treatment context, aptamers are chemically synthesized single-stranded DNA or RNA oligonucleotides capable of binding diverse molecular targets with high affinity and specificity [8]. Their thermal stability, low cost, biocompatibility, and versatility make them valuable tools in biomedical applications such as targeted therapy, biosensing, diagnostics, and molecular imaging [9]. The guanine-rich AS1411 aptamer (AGRO) specifically binds to cell-surface nucleolin, a protein overexpressed in proliferating tumor and angiogenic endothelial cells, thereby exerting antiangiogenic and antitumor effects [10-13]. In this study, samples from untreated control were compared with those from a treatment group receiving a combination of the AGRO aptamer and GK-1, an immunomodulatory peptide whose anti-tumor properties were evaluated on murine experimental melanoma [14-16] and breast cancer [17, 18]. This comparison between groups is used to illustrate the potential of macroscopic Mueller polarimetric imaging for quantitatively assessing treatment-induced changes in the tumor microenvironment (TME) over large tissue areas, while capturing the intrinsic spatial heterogeneity of the samples.

While identifying and characterizing cancer types is crucial for effective treatment and prognosis, Mueller polarimetric imaging has emerged as a quantitative approach in biomedical applications. By analyzing how polarized light interacts with tissue, this method provides access to microstructural and compositional information that is not available through conventional imaging techniques [19,20]. As a result, polarimetric imaging offers a complementary means of examining some aspect of the TME, with sensitivity to features associated with cellular architecture, angiogenesis, and the extracellular matrix. Recent studies have demonstrated the potential of polarimetry as a tool for analyzing different types of malignant neoplasms, including prostate [21], breast [22], cervical [23], colorectal [24, 25], and skin cancers [26,27], and have revealed distinguishable patterns in cancerous cells that could aid in diagnosis and early detection. Previous studies have focused on discrimination between melanoma, other common skin cancer types, and normal skin [26,27], whereas here we quantify macroscopic, wide field heterogeneity of blood vessel– and tumor cell–dominated regions within an already diagnosed melanoma tumor

Specifically, Mueller matrix imaging polarimetry enables comprehensive optical characterization of tissue samples by measuring the polarization properties of light as it interacts with the tissue components. An important advantage of macroscopic Mueller polarimetry is its ability to capture a wide field of view (FOV) when implemented within certain instrumental setups, allowing for the simultaneous analysis of large tissue areas, on the millimeter scale, in a single measurement. This contrasts with traditional histopathological analysis, which relies on high-magnification and narrow microscopic fields of a micrometer scale. Additionally, this examination is often subjective and dependent on the pathologist's knowledge and interpretation [28]. Polarimetric imaging provides quantitative and objective data supporting pathological diagnosis, based on the distinct optical signatures of the heterogeneous TME.

This study presents a macroscopic polarimetric approach for the analysis of selected structural components of the TME in a preclinical murine melanoma model using a complete Mueller matrix imaging polarimeter. The method focuses on the

discrimination between blood vessel–dominated regions and tumor cell–dominated regions within primary melanoma tumors, based on their depolarization behavior. These polarimetric signatures were correlated with histopathological features identified and validated by an experienced pathologist. Rather than aiming at a comprehensive characterization of all TME constituents, the proposed approach targets biologically relevant structures associated with tumor angiogenesis and treatment response. By quantifying the spatial distribution of these structures over several mm^2, the method enables objective, pixel-wise assessment of tissue heterogeneity across large fields of view, substantially exceeding the limited (<1 mm^2) coverage of conventional high-magnification microscopy (40*x*)

This macroscopic polarimetric framework complements standard histopathological evaluation by providing a quantitative and reproducible analysis of vascular and tumor cell organization. By capturing spatial patterns across entire tissue sections, the approach demonstrates its potential for evaluating experimental treatment efficacy and conducting longitudinal studies in preclinical melanoma models.

Materials and methods

Ethical considerations

The research project and the protocols for the bioethical care and use of animals were approved by the Institutional Committee for the Care of Laboratory Animals (CICUAL, per its Spanish acronym) with approval number 029-CIC-2020, and the Research and Bioethics Committees of the Faculty of Medicine at the National Autonomous University of Mexico (UNAM), with approval number FM/DI/086/2020. The ruling of these institutions was in strict accordance with the Mexican norms for animal handling (Norma Oficial Mexicana NOM-062-ZOO-1999) and with international guidelines for animal handling, as outlined in the ARRIVE guidelines (https://arriveguidelines.org).

Animals

18 six-to eight-week-old C57BL/6 male mice were obtained from the animal facilities at the Medicine Faculty, UNAM. The animals were subsequently housed in the animal facility of the Department of Cell and Tissue Biology at the Faculty of Medicine, UNAM, where they were acclimated in the animal house and kept under controlled light (12 hours of light /12 hours of dark) and temperature (22–24 °C) conditions throughout the experiment. Food and water were allowed *ad libitum*.

Melanoma murine preclinical model

The model was similar to the one carried out elsewhere [14-16]. Briefly, B16-F10 tumor cell line, purchased from the American Type Culture Collection (ATCC, Manassas, VA), was grown in RPMI 1640 medium (Gibco, Thermo Fisher Scientific, Waltham, MA) supplemented with 10% fetal heat-inactivated bovine serum (FBS, Gibco) and 1% penicillin and streptomycin (Gibco). Cells were maintained at 37 °C in a humid 5% CO_2 atmosphere and then detached with 0.05% trypsin/0.5 mM EDTA (Gibco) for implantation in mice. At four culture passes, cell line viability was assessed by the trypan blue exclusion method, and $2X10^5$ B16-F10/50 µL of sterile isotonic saline solution was implanted subcutaneously into the flank of each mouse. Two groups were formed: a control group (without treatment), and a group treated with the AGRO/GK-1 combination, the active aptamer AGRO (intratumorally, three times a week, 20 µmol in 50 µL of saline), and the GK-1 peptide (intravenously, 100 µL of a 1 µg/µL solution once a week). Mice were checked three times a week for their clinical status and tumor diagnosis. Only mice that developed a tumor of 20 mm^3, usually 2 weeks after tumor cell implantation (defined as day 0 of the study), were included in the polarimetric analysis. Mice were euthanized with an isoflurane overdose through the "drop method". Briefly, volatile liquid isoflurane (4.6 ml) was dropped on a gauze placed in the conical bottom of a Falcon tube, at room

temperature, approximately 22 °C. The mouse's nose was inserted into the tube; once it was confirmed that there were no vital signs, a cervical dislocation was performed to ensure death. It was strictly established, in accordance with the Guidelines on Choosing an appropriate endpoint in experiments, (recommended by CICUAL-Faculty of Medicine, UNAM), that euthanasia would take place when the tumor reached approximately 2 cm in either length or width or when the mouse showed weight loss for 6 consecutive days or that had lost 20% of weight compared to the beginning of the experiment. During the experiments, the greatest well-being and the least suffering of the mice was always sought.

Samples preparation

After mice were euthanized, primary tumors were obtained, sectioned with a razor blade into fragments of 1 cm thickness, which were fixed by immersion in 10% buffered Zamboni solution, at room temperature for 24 hours. They were then washed in tap water, dehydrated with incremental grades of ethanol until xylene, and paraffin-embedded. Histological sections (4-µm-thick slices) were obtained and stained with hematoxylin & eosin (H&E). For histopathological and polarimetric analysis, H/E-stained tissue sections, separated from each other by 100µm, were used. A total of 51 histological sections were obtained from 18 mice: 25 sections from 9 mice in the control group and 26 sections from 9 mice in the treated group.

Histopathological analysis

Histopathological analysis was performed on paraffin-embedded H&E-stained tissue sections. Slides were imaged using a Zeiss LSM 980 microscope with a 40× objective and an Axiocam 305 digital camera in brightfield mode. Tumor regions were then analyzed by an experienced pathologist and morphologist (P.-T. A.) to identify relevant structures, including tumor cells and intratumoral blood vessels, and to manually delineate these areas. The same tissue regions were subsequently analyzed using the macroscopic polarimetric approach. The histopathological assessment relied on a well-characterized melanoma cell line and the corroboration of key structural features within the primary tumor.

Mueller matrix imaging polarimeter

A Mueller matrix is a 4×4 real matrix, that fully characterizes how a sample modifies the polarization state of light. It encodes key optical properties such as diattenuation, retardance, and depolarization. This formalism operates through the Stokes vector, which describes the polarization state of a light beam and has complete information of the behavior of its electric field in a compact mathematical form [29]. The alteration between the input S_{in} and output S_{out} Stokes vectors is expressed through the following linear transformation:

$$S_{out} = MS_{In};\begin{pmatrix} S_0' \\ S_1' \\ S_2' \\ S_3' \end{pmatrix} = \begin{pmatrix} m_{00} & m_{01} & m_{02} & m_{03} \\ m_{10} & m_{11} & m_{12} & m_{13} \\ m_{20} & m_{21} & m_{22} & m_{23} \\ m_{30} & m_{31} & m_{32} & m_{33} \end{pmatrix} \begin{pmatrix} S_0 \\ S_1 \\ S_2 \\ S_3 \end{pmatrix} \quad (1)$$

where **M** is the sample's Mueller matrix, where each matrix element m_{ij} codifies physical information about how the medium alters the polarization state of light, providing a full description of light–matter interactions, in terms of its electric field.

To acquire spatially resolved Mueller matrices from tissue samples, we employed a Mueller matrix polarimetric imaging system. The system was illuminated using a light-emitting diode (LED) source equipped with a 554 nm band-pass filter to narrow the spectral bandwidth of the illumination. The filtered light was then collimated using a collimating lens (L1) and directed toward the polarization state generator (PSG). The PSG consisted of a linear polarizer with transmission axis oriented at 0º (P1) followed by two liquid crystal variable retarders (LCVR1 and LCVR2), with their fast axes oriented at 45° and 0°, respectively, allowing the generation of arbitrary fully polarized input polarization states.

After interacting with the sample, the light passed through the polarization state analyzer (PSA). The PSA consisted of a liquid crystal variable retarder (LCVR3), with its fast axis oriented at 45°, followed by an imaging lens that focused the transmitted light onto a polarimetric camera (CS505MUP, Thorlabs), equipped with an integrated four-directional wire-grid polarizer array. The micro-polarizers on the sensor were oriented at 0°, 45°, 90°, and 135°, enabling the simultaneous measurement of four polarization projections in a single acquisition. The system uses liquid-crystal variable retarders (LCVRs) for compact, electrically tunable polarization control, combined with a polarization-sensitive camera that acquires four polarization states simultaneously, reducing the number of measurements and overall acquisition time. The polarimeter is compact and portable, comprising a PSG and PSA, each measuring 24 cm length and separated by 10 cm, for an overall footprint of approximately 58 cm × 16 cm × 6 cm. This design is compatible with standard laboratory environments and does not require specialized infrastructure. The system acquires the 8 intensity images needed for Mueller matrix reconstruction in ~2 seconds (≈260 ms per image), with subsequent computation completed in ~9 seconds. Such acquisition and processing times are practical for routine preclinical tissue analysis. Finally, the imaging system is capable of capturing images with a field of view of 89 mm^2 (9.46 × 9.46 mm^2), with an effective spatial resolution of ~14 µm per pixel. The schematic diagram and experimental set-up of the Mueller imaging polarimeter are shown in Fig. 1.

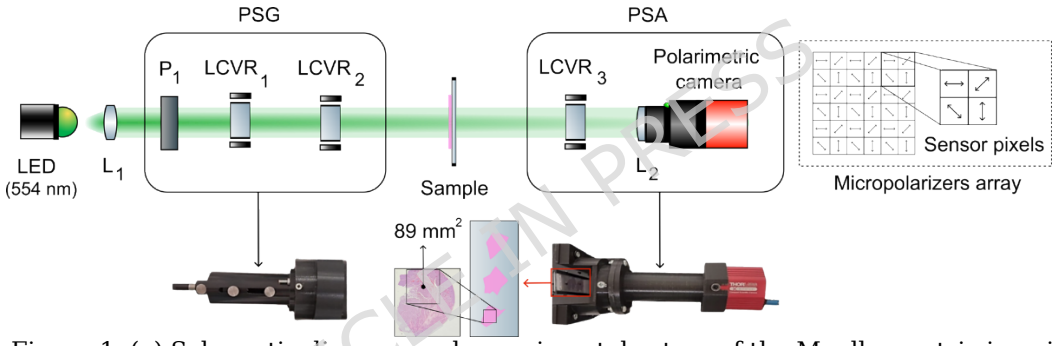

Figure 1. (a) Schematic diagram and experimental set-up of the Mueller matrix imaging polarimeter, including the PSG, sample, PSA.

To retrieve the full Mueller matrix at each pixel of the image a set of independent polarization states, optimized to reduce the error propagation and maximize the signal-to-noise ratio, was generated and analyzed using the PSG and PSA, respectively [30]. The PSG configurations define a set of four known input Stokes vectors, which can be arranged as columns in a 4×4 matrix $\boldsymbol{G}$. Similarly, the PSA configurations define a set of eight analyzed polarization states, represented as rows in an 8×4 matrix $\boldsymbol{A}$. For each combination of input and output polarization states, an intensity image was acquired, resulting in an 8×4 matrix $\boldsymbol{I}$, where each element corresponds to the measured intensity at a given pixel. The measured intensity data is related to the Mueller matrix $\mathbf{M}$ of the sample at each pixel through the polarimetric equation [29]:

$$I = AMG. \tag{2}$$

By solving, for each pixel, this system as

$$M = A^{+}IG^{-1}, \tag{3}$$

where G^{-1} represents the inverse matrix of G and A^{+} the pseudo inverse matrix of A, the full 4×4 Mueller matrix was reconstructed across the entire field of view, providing spatially resolved polarimetric information of the histological sections of the primary tumor.

System calibration and validation were performed, using the Eigenvalue Calibration Method [31], with reference samples of known Mueller matrices, compensating for

cumulative optical non-idealities. After calibration, the condition numbers of the PSG and PSA were 1.98 and 2.70, respectively. Validation of the system was performed using reference samples, obtaining mean absolute errors of 0.060 ± 0.014 for linear polarizers and 0.153 ± 0.046 for quarter-wave plates. Further details on the system implementation and validation are provided in [32]. Potential confounders, including section thickness, H&E staining, and illumination nonuniformity, were controlled through standardized sample preparation and calibration procedures ensuring that the measurements remain reliable.

Following the acquisition of the Mueller matrix, for each sample, we performed a pixel-wise analysis using standard polarimetric decomposition techniques. In this work the analysis focuses on a single polarimetric parameter, the depolarization index (P_Δ), based on prior studies and practical considerations. Retardance-related metrics provided limited structural contrast in the histological sections and were confounded by spatially heterogeneous birefringence introduced by the glass slides. Dichroism-related metrics, while potentially informative in other contexts, exhibited low magnitude in these samples and did not contribute additional discrimination value. More complex depolarization descriptors, such as indices of polarimetric purity did not provide further discrimination due to the predominantly isotropic depolarization observed. In contrast, PΔ demonstrated sufficient robustness and discriminatory power for histopathological relevant structures in the TME (blood vessels and tumor cell–dominated regions), making it appropriate for the scope of this study. The depolarization index was calculated as [29],

$$P_\Delta = \sqrt{\frac{\sum_{i,j=0}^{3} m_{ij}^2 - m_{00}^2}{3m_{00}^2}};\ 0 \le P_\Delta \le 1 \tag{4}$$

where m_{ij} are the elements of the Mueller matrix. The limiting cases are $P_\Delta = 1$, which indicates a non-depolarizing sample, and $P_\Delta = 0$, which corresponds to a fully depolarizing sample (maximal depolarization). Therefore, higher P_Δ values indicate lower depolarization [29]. Depolarization index maps were generated and used for statistical comparison and classification analysis.

Segmentation of tissue structures based on polarimetric thresholding

Based on the distinct depolarizing responses observed across different structures within the TME, a targeted image processing strategy was implemented for the segmentation of relevant tissue components. Depolarization thresholds were defined using regions of interest (ROIs) corresponding to biologically well-defined structures, blood vessel–dominated and tumor cell–dominated regions, independently identified by an experienced pathologist. ROIs were randomly selected across different tumor regions, histological sections, and animals to obtain representative depolarization ranges for each structure. This structure-based approach was chosen to characterize intrinsic optical properties of the tissue components of interest, rather than relying on global image histograms, which depend strongly on the specific composition of each sample and may vary with vascular density or tumor heterogeneity.

Using pixel-wise thresholding of the $P_\Delta(x,y)$maps, four categories were defined based on their depolarization behavior: weakly-depolarizing tissue, transitional tissue, strongly-depolarizing tissue, and non-depolarizing background. For each category, a specific P_Δ range was established (threshold values derived from the statistical analysis of representative ROIs; see Results section). Each range was then used to generate a binary mask, where pixels within the range were assigned a specific color. The final mask combines 4 binarized images of P_Δ, each associated with a different color, such that the complete image is built following

$$P_\Delta(x,y) = P_{\Delta,\text{red}}(x,y) + P_{\Delta,\text{blue}}(x,y) + P_{\Delta,\text{green}}(x,y) + P_{\Delta,\text{dark brown}}(x,y). \tag{5}$$

Each binarized component $P_{\Delta,color}(x,y)$ corresponds to a specific range of P_Δ values associated with a tissue category. The exact thresholds values used are shown in table 1

Table 1. Depolarization threshold ranges used for tissue classification.

Tissue type	Lower bound	Upper bound
Weakly depolarizing tissue	0.879	0.979
Transitional tissue	0.489	0.878
Strongly depolarizing tissue	0.118	0.488

This strategy ensured that each pixel (x,y) was uniquely assigned to a single-color class, enabling objective and reproducible quantification of tissue composition across the full widefield histological section. The full methodology is schematically shown in Fig. 2.

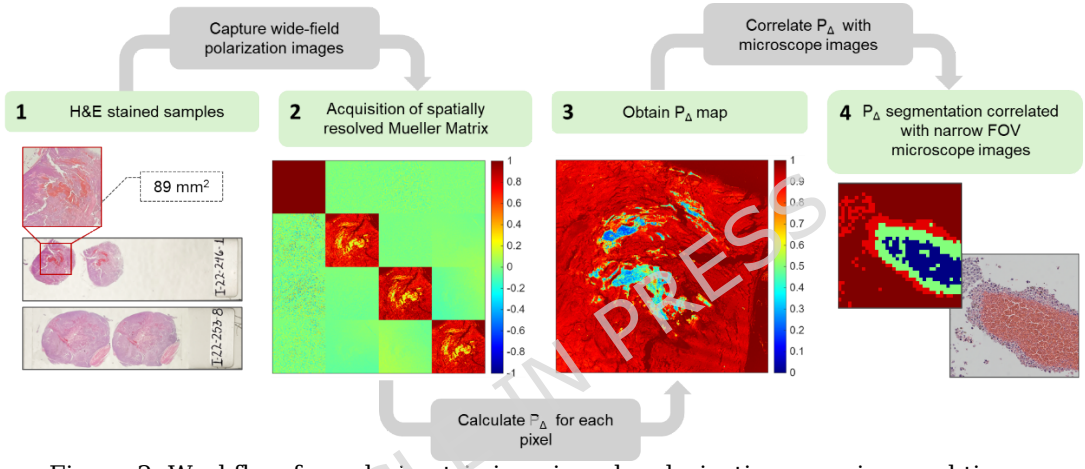

Figure 2. Workflow for polarimetric imaging, depolarization mapping, and tissue assignment.

Results and discussion

Wide-field polarimetric image analysis

To characterize the optical response of the primary tumor of melanoma, we performed wide-field Mueller matrix polarimetric imaging on histological sections from a preclinical murine model. Fig. 3 (a) shows representative whole-tumor sections, with red boxes highlighting the regions (89 mm²) selected for polarimetric analysis. Fig. 3 (b) presents the corresponding Mueller matrix-derived depolarization index images (89 mm²). In the colormaps shown, a wide range of P_Δ values can be observed, from dark red to dark blue, covering nearly the entire range $0 \leq P_\Delta \leq 1$, which reflects significant microstructural and compositional heterogeneity within the TME. Across the full dataset (26 histological sections), dark red areas with $0.98 \leq P_\Delta \leq 1$ correspond to regions without tumor section. Within the tumor section, maximum values up to $P_\Delta = 0.98$ were found, indicating weakly-depolarizing behavior. This may be attributed to internal optical order, transparency, low-density regions, or reduced scattering that enables reduced polarization mixture through light propagation. In contrast, dark blue regions with minimum values of $P_\Delta = 0.07$ indicate highly depolarizing behavior, likely due to multiple scattering within dense and disordered structures. Intermediate values suggest transitional states between these regimes.

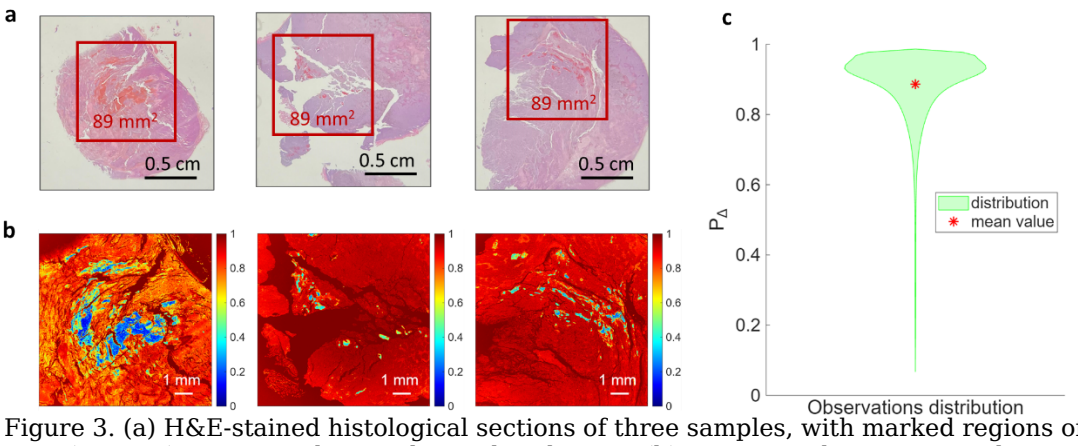

Figure 3. (a) H&E-stained histological sections of three samples, with marked regions of interest (89 mm²) corresponding to the analyzed areas. (b) Corresponding P_Δ maps showing spatial distribution of depolarization across each region. Color scale ranges from 0 (high depolarization, blue) to 1 (non-depolarizing, red). (c) Swarm plot of the distribution of P_Δ values in the complete set of histological sections.

In Fig. 3 (c), a swarm plot of the distribution of P_Δ values, in the complete set of histological sections (28), is presented to visualize the data distribution. The green area represents the density of data points of P_Δ values of the polarimetric images; it can be seen a wide spread of depolarization values, indicating substantial microstructural heterogeneity. Most pixels are concentrated near the non-depolarizing limit, with a mean value of P_Δ=0.89, but a long tail toward lower values reflects the presence of highly depolarizing regions, likely associated with disordered or dense tissue structures, consistent with the visual observation in Fig. 3 (b). These results immediately reveal high spatial heterogeneity in the TME, demonstrating the capability of the polarimetric method to analyze large tissue areas (89 mm²), in a single image.

Correlation of Polarimetric images with histopathological characteristics

Having identified regions of distinct polarimetric behavior, the next step involves investigating the underlying structural origins of the observed optical phenomena. This is achieved by correlating P_Δ maps, with histopathological images obtained via optical microscopy (see Fig. 4 and Fig. 5). This comparison allows for the identification of specific tissue features that contribute to variations in depolarization, thereby providing insight into the microstructural mechanisms influencing the optical response within the TME.

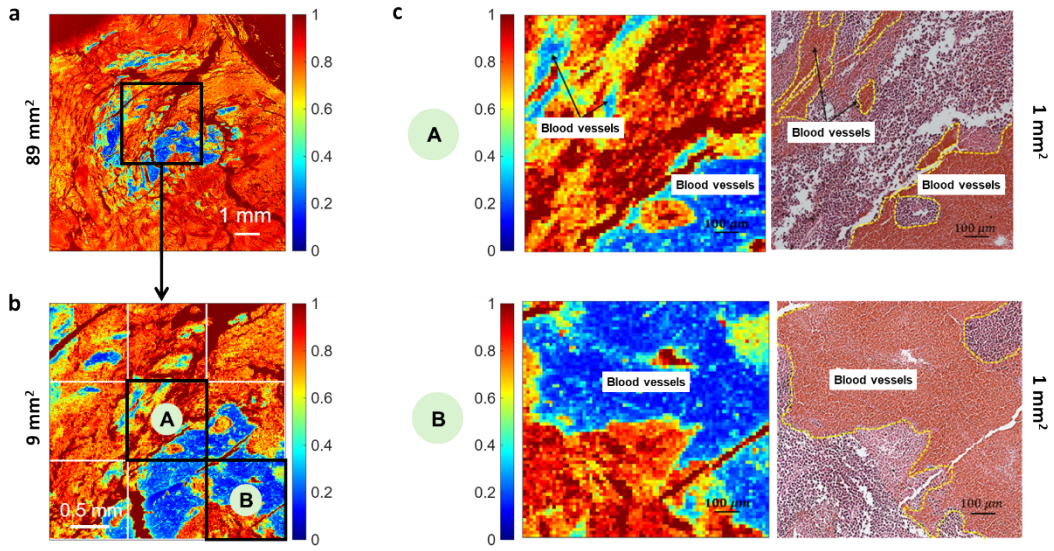

Figure 4. (a) P_Δ map of a representative sample, with a marked region of interest of 9 mm². (b) Zoomed-in P_Δ map showing two selected 1 mm² areas (A and B) with distinct depolarization patterns. (c) Corresponding histopathological images for each region, allowing visual correlation between polarimetric features and tissue structure. Blood vessels are highlighted in yellow dashed lines.

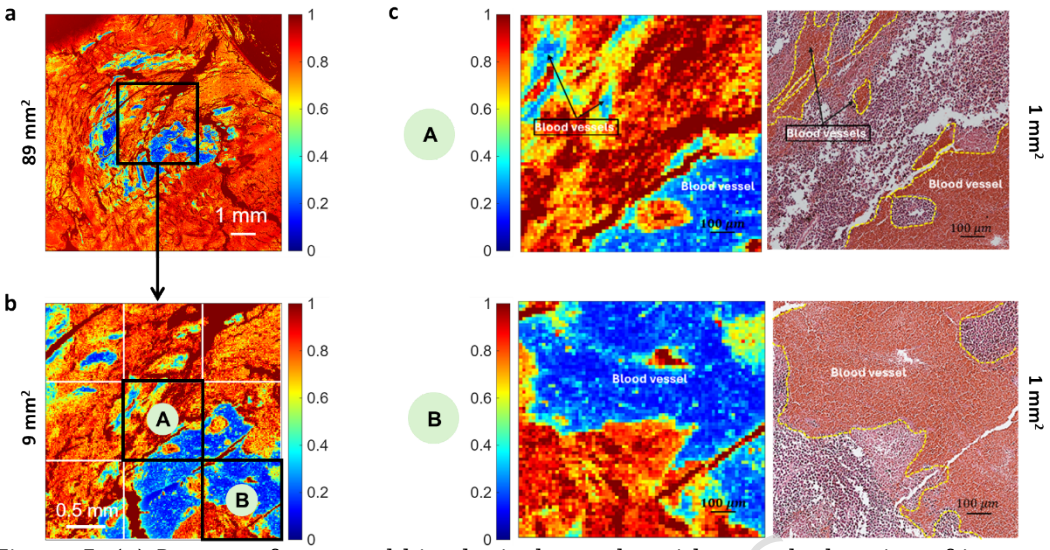

Figure 5. (a) P_Δ map of a second histological sample, with a marked region of interest of 9 mm². (b) Zoomed-in P_Δ map showing two selected 1 mm² areas (A and B) with distinct depolarization patterns. (c) Corresponding histopathological images for each region, allowing visual correlation between polarimetric features and tissue structure. Blood vessels are highlighted in yellow dashed lines.

The qualitative comparison between the polarimetric maps and the corresponding microscope images confirms a clear spatial correlation between depolarization behavior and specific tissue structures. Regions exhibiting low P_Δ values in the polarimetric images (toward dark blue in colormap) correspond to irregular blood vessels (highlighted in yellow dashed line in the histopathological images shown in Fig. 4 and 5 (c) and fine stromal components close to these. While zones with higher P_Δ (toward dark red in colormap) align with more homogeneous tumor cells regions. These results support the idea that depolarization is sensitive to underlying microstructural complexity, justifying a more systematic statistical analysis across multiple ROIs.

To further quantify these correlations, ROIs were selected for statistical analysis. These regions included weakly depolarizing areas corresponding to more organized tumor cells (Figure 6 (a)), and highly depolarizing zones associated with dense vascular structures (Fig. 6 (b)). The morphological features observed in microscope images, such as vessel-like structures or homogeneous, lightly stained regions, serve as reference patterns for grouping the data. Thus, the dataset employed consisted of ROIs covering 67.6 × 67.6 μm², corresponding to zones like the showed in Fig. 6 (a) and (b). These ROIs were identified and selected based on their distinct optical and morphological features observed in polarimetric and histological images, respectively. Only regions that clearly correlated with representative tissue types were included in the dataset, resulting in 36 ROIs per category. To characterize the polarimetric behavior of the distinct tissue components, mean P_Δ values were calculated across the selected ROIs.

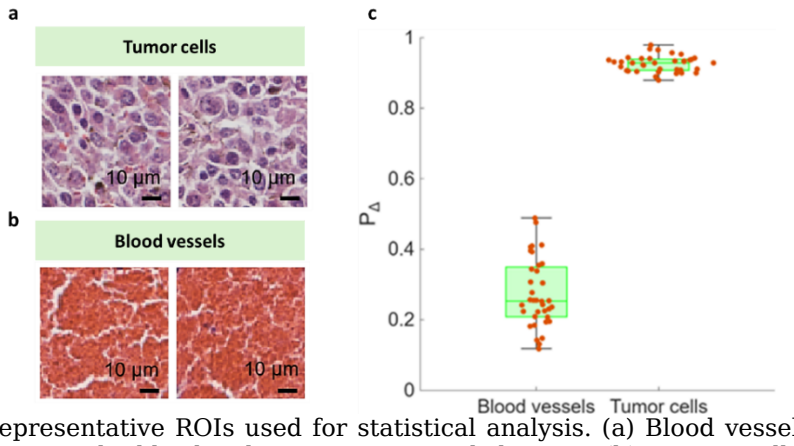

Figure 6. Representative ROIs used for statistical analysis. (a) Blood vessels of primary melanoma tumor are highly depolarizing areas with low P_Δ. (b) Tumor cells are weakly depolarizing zones with high P_Δ. (c) Scattered boxplot of P_Δ values for these two ROIs of TME denotes 36 histopathological images per group. The distributions clearly show distinct depolarization behaviors.

The boxplot shown in Fig. 6 (c) clearly shows two separate distributions, corresponding to different tissue structures, blood vessels and tumor cells, each one exhibiting distinct depolarization responses. Statistical analysis of the data shown in Fig. 6 (c) was performed using a non-parametric rank-sum test. A statistically significant difference between blood vessels and tumor cells was observed ($p = 3.045 \times 10^{-13}$). In addition, the effect size of the rank-sum test ($R = 0.8594$) indicates a strong separation between the two groups. The tumor cells exhibited high P_Δ values from 0.879 to 0.979, with a median value of $P_\Delta = 0.928$, while the blood vessel group showed significantly lower values from 0.118 to 0.488, with a median value of $P_\Delta = 0.253$ reflecting more disordered and scattering regions. Although other ECM components, such as collagen fibers, may exhibit similar high P_Δ values to those observed in tumor cells, collagen-rich stroma is not expected in this preclinical melanocytic melanoma model; therefore, the weakly depolarizing regions are predominantly associated with tumor cells in this context. These findings confirm the potential of depolarization metrics for distinguishing structural features of TME, such as tumor cells and blood vessels. Blood vessels exhibit higher depolarization due to their heterogeneous structure, including red blood cells, which cause multiple scattering and mixing of polarization states. In contrast, tumor cell regions are relatively homogeneous and isotropic, with well-defined nuclei and cytoplasm, allowing polarized light to traverse them with less depolarization. This physical basis explains the observed differences in depolarization between these tissue types.

The P_Δ threshold used for segmentation was chosen based on representative ROIs and corresponds well to histologically identified blood vessels, supporting its relative specificity within this melanoma model. For more complex tissue architectures, where multiple structures may exhibit overlapping P_Δ values, additional polarimetric parameters, such as retardance, diattenuation, or indices of polarimetric purity, could be exploited to further discriminate tissue types. All analyses were performed on H&E-stained samples; therefore, variations in staining may affect optical properties. Nevertheless, our approach captures the overall macroscopic optical response of histologically processed tissue, enabling quantitative, wide-field assessment of vascular and tumor cell regions within the melanoma tissue.

Segmented images based on P_Δ thresholding

In this section we apply the segmentation approach based on P_Δ values described in the Materials and methods section. To implement the method, we applied the statistical analysis of representative ROIs previously presented, from where the different P_Δ ranges were assessed, allowing us to classify tissue structures according to their depolarization response. In particular, pixels with P_Δ values below 0.49 were

associated with strongly depolarizing regions of irregular blood vessels, while weakly-depolarizing tissue, associated with tumor cells, was defined by P_Δ values ranging from 0.88 to 0.98. Those pixels with P_Δ values between 0.49 and 0.88 corresponded to transitional zones of perivascular tumor cells or newly formed blood vessels, and values equal to or above 0.98 were attributed to background areas or without tissue section. Applying these thresholds to the full-field depolarization maps allowed the generation of segmented images in which each pixel is uniquely assigned to one category. This segmentation enabled spatial quantification and objective comparison of tissue components across entire histological sections.

The second column of Fig. 7 (a) shows a wide-field view of 89 mm², where each pixel was classified and color-coded based on its depolarization behavior, in the first column the corresponding histological section is presented. In this representative example, 82.1% of the tissue area was classified as weakly depolarizing, 1.7% as strongly depolarizing, and 16.2% as transitional regions. In these percentages, the background, regions without tissue, are not considered. To assess local variability, next to the wide-field view a zoomed-in 1 mm² field of view is presented, from the same section, alongside the corresponding histopathological image. In this smaller region, the proportions changed considerably: 47.0% weakly depolarizing, 18.5% strongly depolarizing, and 34.5% transitional. These differences illustrate the high spatial heterogeneity of the TME and highlight the importance of using large fields of view, as localized analysis can yield significantly different interpretations depending on the area observed, as is often the case in routine histopathological analysis, unless numerous sections of the sample are available. Moreover, a significant amount of time is spent on observation of a limited FOV using the microscope. In Fig. 7 (b) a second histological section was analyzed in the same way. While the overall distribution in the wide-field view was similar in terms of proportions, analysis of selected areas again revealed distinct percentages, further reinforcing the relevance of field size when analyzing the TME.

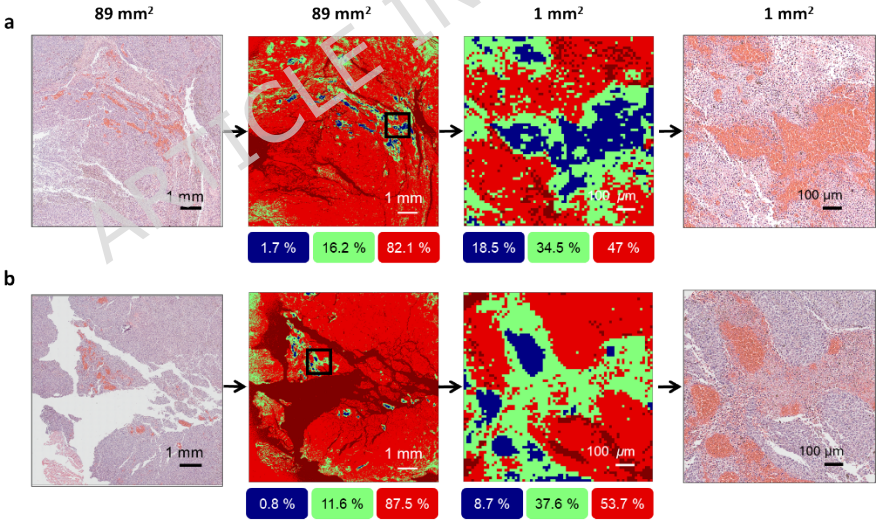

Figure 7. Two representativehistological sections, (a) and (b), with the wide-field polarimetric analysis (89 mm²) using a mask to highlighting three ROIs (blue, green, and red) of melanoma TME based on P_Δ values: weakly depolarizing (tumor cells away from blood vessels), strongly depolarizing (irregular blood vessels), and transitional regions (perivascular tumor cells). Also magnified view (1 mm²) of a selected area, showing both the masked polarimetric map and correlative histopathological image. Here, the relative proportions changed, illustrating local heterogeneity due to a non-random sampling.

Threshold robustness was evaluated by varying the selected values within ±2% of the full depolarization index range. Under these variations, the relative proportion of vascular regions changed by less than 0.7%, in the 1 mm² images, indicating stable segmentation results. This procedure rather than focusing on local structure identification, the proposed wide-field polarimetric approach enables objective

quantification of the relative abundance of vascular and tumor cell–dominated regions across entire tissue sections, complementing conventional histopathological assessment. As mentioned before, each pixel is uniquely assigned to a single color in the retrieved image from the segmentation approach, corresponding to a specific tissue structure based on its depolarization behavior. To illustrate this classification at the pixel level, Fig. 8 presents three randomly chosen 5×5-pixel regions. Fig. 8 (a) shows the classified regions with color-coded pixels indicating distinct depolarization (structures) responses, while panel (b) displays the corresponding histological images. Each colored block in the segmented maps highlights a distinct optical response, clearly aligning with morphological features in the histology images. This visualization was validated through the full FOV and confirms that the classification model accurately captures local tissue heterogeneity with high spatial precision.

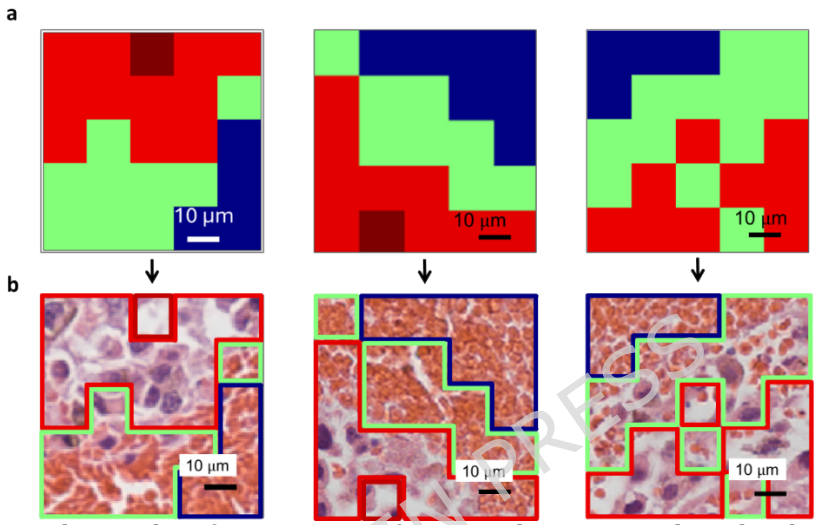

Figure 8. (a) Pixel-wise classification maps of 5×5 pixel regions, with each color representing a distinct depolarization response. Tissue classes are color-coded as follows: weakly depolarizing (red pixels) predominantly corresponds to tumor cell–dominated regions, transitional (green pixels) represents mixed tissue including perivascular areas and occasional tumor or inflammatory cells, and strongly depolarizing (blue pixels) correspond to blood vessels. (b) Corresponding H&E-stained histological images showing morphological features that align with the classification maps.

This qualitative validation against expert histopathological assessment was performed at multiple spatial scales, including representative 1 × 1 mm² regions (Fig. 7) and pixel-level comparisons over ~70 × 70 µm² areas (Fig. 8), confirming the biological relevance of the polarimetric discrimination. In Fig. 8, WD regions (red pixels) are predominantly composed of tumor cells, consistent with the expected histology of the B16F10 melanoma model, which does not present collagen-rich stroma. T regions (green pixels) represent mixed tissue, including occasional tumor or inflammatory cells and perivascular areas with red blood cells and several white blood cells, while SD regions (blue pixels) correspond uniquely to blood vessels.

A limitation of this method is that the wide-field configuration provides lower spatial resolution compared with microscopy. Although microstructural details cannot be directly resolved, they are indirectly captured through the optical response of 14 µm × 14 µm microstructural areas, generating depolarization signatures that enable large-tissue area quantitative analysis. To summarize the full dataset, a cumulative quantification of all analyzed sections from the preclinical melanoma model is presented in Table 2. A total tissue area of 1726 mm² was examined, with each pixel classified according to its depolarization behavior. Of this area, 1185 mm² (≈69%) corresponded to weakly-depolarizing tissue, 674 mm² (≈30%) to transitional zones, and 18 mm² (≈1%) to strongly depolarizing structures. These results provide a comprehensive spatial breakdown of the TME, confirming the predominance of weakly depolarizing regions of tumor cells alongside the presence of irregular blood

vessels, which reflect the structural complexity of the TME and further supporting the potential of polarimetric imaging for large-scale tissue characterization.

Table 2. Summary of the total analyzed area and the corresponding distribution of tissue types based on their depolarization behavior. Values are reported in mm², calculated from the full set of histological sections acquired from the preclinical melanoma model.

Tissue type	# Pixels	Total area (mm²)
Total tissue analyzed	8,809,783	1726
Strongly depolarizing tissue	93,329	18
Transitional tissue	2,669,822	523
Weakly-depolarizing tissue	6,046,632	1185

Depolarization analysis under different treatment conditions

Understanding how therapeutic strategies influence the tumor TME is essential for evaluating treatment efficacy and identifying reliable optical biomarkers. In this context, this study demonstrates the potential of the depolarization index and associated image processing to detect structural changes associated with tumor response to treatment with two antitumor agents. Building on these findings, we aim to evaluate whether polarimetric methods can also estimate the impact of therapeutic treatments on TME, thereby offering a quantitative approach to monitor treatment-induced alterations. To evaluate treatment-specific optical signatures, a comparative analysis of P_Δ was performed for the two experimental groups. The combination of the AGRO aptamer and the GK-1 peptide is expected to inhibit angiogenesis and reduce tumor cell population through complementary mechanisms [6,18]. A total tissue area of 1163 mm² was examined in the treatment group and was compared with an untreated control group, which represents the baseline tumor condition.

A quantitative analysis was conducted on full-section data from nine animals per group, calculating the relative area of each tissue classification. As summarized in Fig. 9 (a), strongly depolarizing (SD) tissue represents 1.1% in the control group and decreased significantly to 0.3% in the AGRO/GK-1 melanoma treated group, suggesting a reduction in vascular structures consistent with the expected antiangiogenic effect of the treatment [18, 33]. Transitional tissue (T) also decreased from 30.3% in controls to 24.3% in treated tumors, indicating a lower proportion of stromal components, newly formed blood vessels, and perivascular tumor cells. Conversely, weakly-depolarizing tissue (WD) increased from 68.6% to 75.4%, reflecting a potentially more homogeneous tissue and a relative increase due to reduced vascular components, rather than an absolute rise in tumor cell number. To further support these observations, per-animal analysis reveals meaningful trends consistent with an anti-angiogenic effect: These results showed fewer treated animals (1 of 9) with substantial vascularization (>1% tumor area) compared with controls (3 of 9), while more treated animals (3 of 9) had negligible vascularization (<0.1%) versus controls (1 of 9), consistent with an anti-angiogenic effect.

Fig. 9(b) shows the boxplots corresponding to the distribution of P_Δ values for each tissue class in both the control and AGRO/GK-1–treated groups. The treatment produced slightly higher mean P_Δ values, increasing from 0.34 to 0.38 in the strongly depolarizing regions and from 0.82 to 0.85 in the transitional regions, while remaining unchanged in the weakly-depolarizing regions. Changes in distribution width were also observed across tissue classes. In the strongly depolarizing regions, the whisker width decreased from 0.41 in the control to 0.37 in the treated group. Similarly, in the transitional regions, the whisker width was reduced from 0.25 to 0.16, whereas in the weakly-depolarizing regions, it remained nearly identical (0.10 in both conditions). The narrower distributions indicate reduced variability within

each tissue class. This effect was more evident in the transitional regions, corresponding to stromal and perivascular areas, suggesting local structural reorganization. Strongly depolarizing regions, associated with irregular vascular structures, also exhibited lower dispersion in the treated group, which may indicate decreased microstructural heterogeneity, potentially reflecting a more uniform matrix organization. Meanwhile, the weakly-depolarizing regions maintained the mean value and P_Δ distribution, in both groups, supporting the presence of a stable and homogeneous microstructural organization.

Statistical comparisons between control and treatment groups were performed per tissue category using a non-parametric rank-sum test. Pixel-wise p-values were extremely small ($p < 2.15 \times 10^{-19}$) due to the large number of measurements, so the rank-sum effect size (R) was also reported. For weakly depolarizing tissue (tumor cells) R = 0.10, and for strongly depolarizing tissue (blood vessels) R = 0.09, indicating that the intrinsic polarimetric signatures remain unchanged after treatment. The transitional tissue category showed a higher effect size (R = 0.22), consistent with its heterogeneous composition and the fact that it does not correspond to a single well-defined tissue structure or classified region, reflecting mixed optical responses from multiple tissue components. These results confirm that P_Δ reliably discriminates tissue types and that treatment effects are captured by changes in the relative abundance of each tissue type rather than by changes in their optical properties. Overall, these findings highlight the utility of polarimetric imaging to quantify the relative proportions of vascular and tumor tissue, providing an objective measure of treatment efficacy.

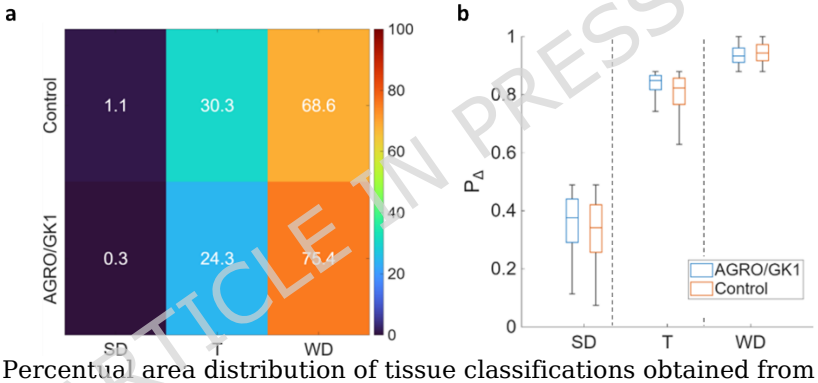

Figure 9. (a) Percentual area distribution of tissue classifications obtained from full-section polarimetric data for control and AGRO/GK-1–treated melanoma groups. Tissue classes are color-coded as follows: weakly depolarizing (WD) predominantly corresponds to tumor cell–dominated regions, transitional (T) represents mixed tissue including perivascular areas and occasional tumor or inflammatory cells, and strongly depolarizing (SD) correspond to blood vessels. (b) Box plot of the depolarization index (P_Δ) for each tissue class, comparing control and AGRO/GK-1 groups.

Conclusions

This work proposes a quantitative methodology based on Mueller matrix polarimetric imaging for the analysis of histological sections, using the depolarization index, P_Δ, to discriminate specific tissue microstructure. By combining pixel-level polarimetric information with a segmentation strategy, the approach enables an objective, quantitative, and reproducible classification of tissue regions that are often challenging to assess through conventional visual inspection alone. Rather than assigning an optical parameter to a specific biomolecular component, the present study quantifies statistically validated optical compartments that are independently confirmed by histopathology. Within the biological context of the antiangiogenic therapeutic effects investigated, vascular quantification represents the most relevant and robust structure.

A key strength of the method is its wide field of view, which allows the analysis of large tissue areas within histological sections. This capability is particularly relevant given the pronounced heterogeneity of tumor tissues, where narrow FOV assessments, such as conventional microscopy, may overlook relevant structures located outside the inspected region. The comparison between wide-field and

localized analyses further demonstrates that tumors exhibit marked spatial variability in their TME characteristics and depolarization behavior. These results highlight the importance of extended-area evaluation to obtain a representative characterization of the TME and to reduce sampling bias inherent to small-field observations.

As a practical application, the proposed methodology was applied to compare depolarization patterns in untreated and treated tumors in a murine melanoma model. The analysis enabled discrimination between blood vessel–dominated and tumor cell–dominated regions and allowed quantification of their relative abundance over entire tissue sections. The observed differences between groups demonstrate that wide-field polarimetric imaging can capture treatment-related changes in tumor vascularization and microenvironmental organization, supporting its utility for quantitative assessment of treatment effects in preclinical studies.

References

1. Martínez-Jiménez F, Muiños F, Sentís I, Deu-Pons J, Reyes-Salazar I, Arnedo-Pac C, Mularoni L, Pich O, Bonet J, Kranas H, Gonzalez-Perez A, Lopez-Bigas N. A compendium of mutational cancer driver genes. Nat Rev Cancer. (2020) 20:555–72. doi: 10.1038/s41568-020-0290-x
2. Vitale I, Shema E, Loi S, Galluzzi L. Intratumoral heterogeneity in cancer progression and response to immunotherapy. Nat Med. (2021) 27(2):212-224. doi: 10.1038/s41591-021-01233-9.
3. Kim IS, Zhang XH. One microenvironment does not fit all: heterogeneity beyond cancer cells. Cancer Metastasis Rev. (2016) 35(4):601-629. doi: 10.1007/s10555-016-9643-z.
4. Katsuta E, Rashid OM, Takabe K. Clinical relevance of tumor microenvironment: immune cells, vessels, and mouse models. Human Cell. (2020) 33, 930–937. doi 10.1007/s13577-020-00380-4.
5. Arnold M, Singh D, Laversanne M, Vignat J, Vaccarella S, Meheus F, Cust AE, de Vries E, Whiteman DC, Bray F. Global burden of cutaneous melanoma in 2020 and projections to 2040. JAMA Dermatol. (2022) 158(5):495-503. doi: 10.1001/jamadermatol.2022.0160.
6. Wu, Z., Bian, Y., Chu, T., Wang, Y., Man, S., Song, Y., & Wang, Z. The role of angiogenesis in melanoma: Clinical treatments and future expectations. Front Pharmacol. (2022) 13, 1028647. doi.org/ 10.3389/fphar.2022.1028647.
7. Turlej E, Domaradzka A, Radzka J, Drulis-Fajdasz D, Kulbacka J, Gizak A. Cross-Talk between cancer and its cellular environment-A role in cancer progression. Cells. (2025) 14(6):403. doi: 10.3390/cells14060403.
8. García Melián MF, Moreno M, Cerecetto H, Calzada V. Aptamer-Based Immunotheranostic Strategies. Cancer Biother Radiopharm. 2023 May;38(4):246-255.
9. Odeh F, Nsairat H, Alshaer W, Ismail MA, Esawi E, Qaqish B, Al Bawab A, Ismail SI. Aptamers chemistry: Chemical modifications and conjugation strategies. Molecules 2020.
10. Shi H, Huang Y, Zhou H, Song X, Yuan S, Fu Y, Luo Y. Nucleolin is a receptor that mediates antiangiogenic and antitumor activity of endostatin. Blood 2007, 110, 2899–2906.
11. Huang Y, Shi H, Zhou H, Song X, Yuan S, Luo Y. The angiogenic function of nucleolin is mediated by vascular endothelial growth factor and nonmuscle myosin. Blood 2006, 107, 3564–3571.

12. Rosenberg JE, Bambury RM, Van Allen EM, Drabkin HA, Lara PN Jr, Harzstark AL, Wagle N, Figlin RA, Smith GW, Garraway LA, Choueiri T, Fredrik Erlandsson F, Laber DA. A phase II trial of AS1411 (a novel nucleolin-targeted DNA aptamer) in metastatic renal cell carcinoma. Investig. New Drugs 2014, 32, 178–187.
13. Reyes-Reyes EM, Šalipur FR, Shams M, Forsthoefel MK, Bates PJ. Mechanistic studies of anticancer aptamer AS1411 reveal a novel role for nucleolin in regulating Rac1 activation. Mol. Oncol. (2015), 9, 1392–1405.
14. Pérez-Torres A, Vera-Aguilera J, Hernaiz-Leonardo JC, Moreno-Aguilera E, Monteverde-Suarez D, Vera-Aguilera C, Estrada-Bárcenas D. The synthetic parasite-derived peptide GK1 increases survival in a preclinical mouse melanoma model. Cancer Biother Radiopharm. (2013) 28(9):682-690.
15. Pérez-Torres A, Vera-Aguilera J, Sahaza JH, Vera-Aguilera C, Moreno-Aguilera E, Pulido-Camarillo E, Nuñez-Ochoa L, Jeganathan P. Hematological Effects, Serum, and Pulmonary Cytokine Profiles in a Melanoma Mouse Model Treated with GK1. Cancer Biother Radiopharm 30(6):247-254, 2015. DOI 10.1089/cbr.2015.1835.
16. Vera-Aguilera J, Perez-Torres A, Beltran D, Villanueva C, et al. Novel Treatment of Melanoma: Combined Parasite-Derived Peptide GK-1 and Anti-Programmed Death Ligand 1 Therapy. Cancer Biother Radiopharm (2017) 32(2):49-56. doi 10.1089/cbr.2016.2123.
17. Torres-García D, Pérez-Torres A, Manoutcharian K et al (2017) GK-1 peptide reduces tumor growth, decreases metastatic burden, and increases survival in a murine breast cancer model. Vaccine 35:5653–5661. https:// doi. org/ 10. 1016/j. vaccine. 2017. 08. 060.
18. Hernández-Aceves JA, Cervantes-Torres J, Torres-García D, Zuñiga-Flores FJ, Patiño-Chávez OJ, Peña Agudelo JA, Aguayo-Flores JE, Garfias Y, Montero-León L, Romero-Romero L, Pérez-Torres A, Fragoso G, Sciutto E. GK-1 effectively reduces angiogenesis and prevents T cell exhaustion in a breast cancer murine experimental model. Cancer Immunol Immunother. 72(11):3825-3838. doi: 10.1007/s00262-023-03538-9. 2023)
19. Alali S, Vitkin IA. Polarized light imaging in biomedicine: emerging Mueller matrix methodologies for bulk tissue assessment. J Biomed Opt. (2015) 20(6): 061104.
20. C. He, H. H. He, J. Chang, B. G. Chen, H. Ma, and M. J. Booth, “Polarisation optics for biomedical and clinical applications: a review,” Light Science and Applications, (2021), 10: 194.
21. Badieyan S, Ameri A, Razzaghi MR, Rafii-Tabar H, Sasanpour P. Mueller matrix imaging of prostate bulk tissues; polarization parameters as a discriminating benchmark. Photodiag Photodyn Ther. (2019) 26: 90-96.
22. Thi-Thu-Hien Pham et.al. Analysis of polarization features of human breast cancer tissue by mueller matrix visualization. Journal of Biomedical Optics, 29, (2024).
23. Nishkarsh Kumar et. al. Mueller matrix-based characterization of cervical tissue sections: a quantitative comparison of polar and differential decomposition methods. Journal ofBiomedical Optics, 29, (2024).
24. Tumanova K, Serra S, Majumdar A, Lad J, Quereshy F, Khorasani M, Vitkin A. Mueller matrix polarization parameters correlate with local recurrence in patients with stage III colorectal cancer. Sci Rep. (2023) 13: 13424.
25. Sharma, M., Unni, S.N., Shaji, C. et al. Characterizing colon cancer stages through optical polarimetry-assisted digital staining. Lasers Med Sci 39, 59 (2024)
26. Vahidnia A, Madanipour K, Abedini R, Karimi R, Sanderson J, Zare Z, Parvin P. Quantitative polarimetry Mueller matrix decomposition approach

for diagnosing melanoma and non-melanoma human skin cancer. OSA Continuum. (2021) 4, 2862-2874.
27. V. N. Du Le and Austin Bolden, "Cost-effective Mueller matrix microscopy for label-free differentiation of melanoma from normal skin and common skin cancer types," Biomed. Opt. Express 16, 5235-5247 (2025)
28. Nakhleh RE, et al. Interpretive diagnostic error reduction in surgical pathology and cytology: guideline from the College of American Pathologists Pathology and Laboratory Quality Center and the Association of Directors of Anatomic and Surgical Pathology. Arch. Pathol. Lab. Med. (2016); 140:29–40.
29. Chipman R. A., “Handbook of Optics,” New York, McGraw-Hill, 1995: Ch. 22.
30. Montes-González I, Rodríguez-Herrera O. G, Avendaño-Alejo M, and Bruce N. C, “Effects of typical liquid-crystal retarder errors on optimized Stokes polarimeters,” Applied Optics, 2022, 61(35): 10458–10464
31. Montes-Gonzalez I, Estévez I, Canabal-Carbia M, et al. Generalized Eigenvalue Calibration Method for Mueller Imaging Polarimeters Based on Micro-Polarized Sensors With Optimal Set of Calibration Samples. Photonic Sens 15, 250320 (2025).
32. Montes-González I., Campos J., Estévez I, Lizana A., "Modeling and validation of a Mueller matrix imaging polarimeter based on liquid crystals and a polarimetric camera," Proc. SPIE 13568, Modeling Aspects in Optical Metrology X, 135680N (8 August 2025).
33. Vivanco-Rojas O, García-Bermúdez, MY, Iturriaga-Goyon, E, Rebollo W, Buentello-Volante B, F, Magaña-Guerrero FS, Bates P, Pérez-Torres A, Garfias Y. Corneal neovascularization is inhibited with nucleolin-binding aptamer, AS1411. DOI 10.1016/j.exer.2020.107977. Exp Eye Res 193,107977, 2020.

Funding declaration: This work was financially supported by the Ministerio de Ciencia e Innovación, Fondos FEDER, Spain (Grant Nos. PID2024-156240OBOB-C22, and PDC2022-133332-C21), Generalitat de Catalunya, Spain (Grant No. 2021SGR00138). and DGAPA UNAM through the project PAPIIT: IT201821 (FM/DI/086/2020).

Acknowledgements: The authors acknowledge the optical microscopy service of the Universitat Autònoma de Barcelona, and the histotechnological assistance of Dulce Marlet Morales Sánchez and Damaris Ramírez Hernández.

Data availability statement: The datasets used and/or analysed during the current study available from the corresponding author on reasonable request.

Competing Interests Statement The authors declare that they have no competing interests.

Authors contributions Conceptualization: I.M., A.P. and A.L. Optics and instrumentation: I.M. and J.C. Performed the experiments: J.B., I.M. and I.E. Analyzed the data and prepared all figures: J.B. I.M. and M. C. Provided Mueller imaging motivation and insight: A.L., M.C. and I.E. Supplied the tissue samples: A.P. and E.P. Identified the ROIs for analysis. A.P. I. M. and J. B. Provided clinical motivation and insight: A.P. and E. P. Writing and editing the manuscript: I.M., J.B., A. P. and A.L. Funding acquisition: A.L., J.C. and A.P. All authors participated approved the final document before submission and are responsible for its content.